Augmented Magnetic Response and Spin-Transfer in Copper Corrole/Graphene Hybrids - A DFT Study

Kerry Wrighton-Araneda,[1,2] Diego Cortés-Arriagada,[1] Paulina Dreyse,[3] Simon Pascal,[4]

Gabriel Canard,[4]* and Luis Sanhueza[5,6]*

[1] Programa Institucional de Fomento a la Investigación, Desarrollo e Innovación, Universidad Tecnológica Metropolitana, Ignacio Valdivieso 2409, San Joaquín, Santiago, Chile.

[2] Universidad Bernardo O'Higgins, Centro Integrativo de Biología y Química Aplicada (CIBQA), General Gana 1702, Santiago, Chile, 8370854.

[3] Departamento de Química, Universidad Técnica Federico Santa María, Av. España 1680, Valparaíso, Chile.

[4] Aix-Marseille Univ, CNRS, CINaM, UMR 7325, Campus de Luminy, 13288 Marseille Cedex 09, France.

[5] Departamento de Ciencias Biológicas y Químicas, Facultad de Recursos Naturales, Universidad Católica de Temuco, Temuco, Chile.

[6] Núcleo de Investigación en Bioproductos y Materiales Avanzados (BioMA), Universidad Católica de Temuco, Av. Rudecindo Ortega 02950, Temuco, Chile.

E-mail address: luis.sanhueza@uct.cl; gabriel.canard@univ-amu.fr

Abstract.

The search for hybrid materials with outstanding electronic performance is highly demanding Since copper corroles have emerged as versatile building blocks providing outstanding electronic, and reactivity properties, a new series of non-covalent hybrid materials were computationally investigated based on pristine graphene and A3-type copper corrole complexes. The corrole complexes contain strong electron-withdrawing fluorinated substituents at the *meso* positions. Our results show that the non-innocent character of corrole moiety modulates the structural, electronic, and magnetic properties of the hybrid systems. The graphene-corrole hybrids display outstanding stability *via* the interplay of dispersion and electrostatic driving forces while graphene act as an electron reservoir for more conductive cases. Furthermore, the hybrid structures display an intriguing magneto-chemical performance since a detailed analysis of magnetic properties evidence how structural and electronic changes contribute to the amplification of the magnetic response also for ferromagnetic and antiferromagnetic cases. This amplification is accompanied by the spin transfer which characterized by a directional spin polarization from the corrole through the graphene surface. Main results suggest that graphene-corrole hybrids are excellent candidates for technologic applications due to the ferromagnetic tendency, the augmented magnetic response, the tunability due to substituents, and the potential conductive properties. Finally, a statistical analysis of magnetic properties suggests correlations between spin transfer, augmented magnetic response, and the geometrical distortion of the copper ligand field, offering exciting hints about how to modulate the magnetic response in the studied hybrid systems.

Keywords: Magnetism; corroles; Graphene, Hybrid material, Adsorption,

1. Introduction.

Hybrid materials have emerged as promising materials because of their unique and outstanding properties for several domains and applications, including catalysis [1], optical devices [2,3], environmental [4], medicine [5], energy storage [6], among others. Hybrid materials consist of at least two components of different nature to combine their unique physicochemical properties and bind through covalent or non-covalent interaction [7]. In this context, graphene (G), graphene oxide (GO), doped graphene (DG), and graphene quantum dots (GQDs) has been studied due to their attractive mechanical, electrical, and photophysical properties, which can be complemented in the preparation of graphene hybrid based materials (GBMs) [8–10]. Covalently linked GBMs have been extensively studied, highlighting the particular advantage of the graphene moiety on increased stabilities, charge/discharge kinetics, and capacities, and increased electron transfer processes towards nonlinear optical properties [11–14]. Among the wide variety of adsorbates, macrocyclic compounds such as porphyrins and phthalocyanines appear as attractive candidates to tune up the properties of hybrid materials. For instance, G surfaces coated with Co-porphyrins and Fe-phthalocyanines showed enhancement of electron transfer process, providing highly active materials for oxygen reduction reactions [15]. Besides, high stability and large electron-conductivity of GQDs/Zn-porphyrins hybrids are observed towards photocatalytic degradation of pollutants [16]. G coated by $\pi-\pi$ stacking with a water-soluble phthalocyanine demonstrated large synergism as a photosensitizer suitable for photothermal and photodynamic therapies [17]. Similarly, porphyrin derivatives coated on GO surfaces have shown remarkable fluorescence quenching processes, indicating mostly a fastback electron transfer process on the studied hybrid, in conjunction with a computed interaction of about ~1.0 eV (22 kcal/mol) [18,19].

On the other hand, an increasing interest has been evidenced in the chemistry of corroles and their metallo-derivatives because of their unique photophysical and electrochemical properties [20–22]. Corroles are analogous to porphyrins but lacking the C_{20} *meso*-carbon atom at the core structure, and they have been proposed as suitable compounds in cancer therapy, sensing, organic electronics, and catalysis[23–33]. In this sense, new synthetic strategies for developing corrolic derivatives have been proposed, mainly substituted at the *beta* [23,34,35] and/or *meso* [23,35,36] positions of the corrolic core. Here, electron-withdrawing *meso*-substituents appear as an excellent strategy to increase the stability of the macrocycle, in combination with the modulation of the electron density on the core structure of the corresponding derivatives [37]. Alternatively, the binding of metal cations in the central cavity has also been explored; Fe(IV) and Cu(III) [38–42] corrole complexes have been recognized as exciting metallo-derivatives, where the corrolato moiety acts as a non-innocent ligand. In the particular case of Cu-corroles, this definition implies a rearrangement of the electronic structure of the π-extended macrocycle upon metalation. Accordingly, a partial electron transfer between the metal cation and the corrolic structure occurs, stabilizing the formation of a magnetically coupled corrole$^{2-•}$/Cu(II)$^{•}$ radical pair instead of the formal expected Cu(III) cation [41,43,44]. Thus, quantum chemical calculations show that antiferromagnetic coupling between copper and corroles, which is predominant over the formal singlet closed-shell spin state, e.g., the Cu(III) case [41,45,46]. Despite this, few references involving corroles on non-covalent hybrid GBMs are reported. Cobalt corroles supported on graphene-based surfaces have improved catalytic performances towards hydrogen evolution [47] and oxygen reduction reaction [33]. This behavior is explained according to the strong π-π interactions in the obtained hybrids, high stability, and the fast electron transfer on the hybrid. Despite this evidence, a systematic study of the

electronic and magnetic properties of copper corroles supported on graphene surfaces remains unexplored.

In this work, a series of A$_3$-copper corroles bearing different fluoroalkyl, fluoroalkyl, and vinyl substituents at the *meso* positions are investigated as isolated complexes and their corresponding hybrid systems supported on a pristine graphene sheet (**Fig. 1**). The fluorinated substituents of the studied Cu corroles were selected since they promote the stability of the corrole structure and increase the formal high valent character of the metal center [33,37,47]. Furthermore, the nature of the substituents (noted R on **Fig. 1**) was selected to evaluate the effect of the aryl, alkyl, or vinyl skeleton, as well as the rigidity of the corresponding substituent on the stability of non-covalent interactions. Density functional theory (DFT) calculations were performed to gain insights into the main parameters controlling the occurrence of graphene-corrole hybrids

2. Computational Methods

A hexagonal graphene nanosheet (**G**, $C_{384}H_{48}$) with a diameter of ~39 Å and an area of 2692 Å^2 (based on its electron density) was designed from graphite crystalline structure [48] (**Fig. 1a**). The copper corroles (**CuC**) are substituted on 5, 10, and 15 positions giving rise to **C1-C7** compounds (**Fig 1b**). DFT calculations were performed using the ORCA4 program [49], considering the unrestricted open-shell formalism. The hybrid functional B3LYP [50,51] was used with the 6-31G* basis sets; the LANL2DZ quasi-relativistic pseudo-potential and basis set [52] was adopted for Cu. Energies were corrected for dispersion using the DFT-D3BJ method [53,54].
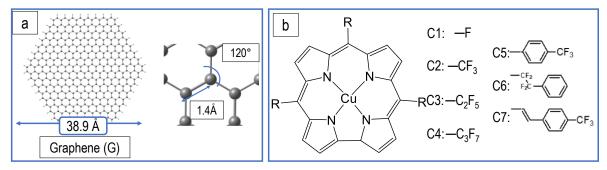
Fig. 1. Molecular structure of (a) Graphene, (b) R substituent groups, and **CuN$_4$** unit for **C1-C7** compounds.

The stability of the graphene and corroles isolated structures were evaluated using cohesive energy. Thus, $E_{coh}=[E_{molecule} - \Sigma n_i E(i)]/(\Sigma n_i)$; where $E_{molecule}$, n_i, and $E(i)$ are the total energy of the molecule, the number of i-atom and the total energy of i-atom forming the molecule, respectively.

The global reactivity indexes [chemical potential (μ), electronic hardness (η), and electrophilicity (ω)] were calculated to evaluate the chemical stability of the proposed systems towards an external perturbation, using the Koopman´s theorem: $\mu = \frac{1}{2}(E_L+E_H)$; $\eta = \frac{1}{2}(E_L - E_H)$; and, $\omega = \mu^2/2\eta$ [55], where E_L and E_H were calculated as the average between energies of α and β spin-orbitals.

The stability of corrole-graphene hybrids (**C-G**) was characterized by the adsorption energies (E_{ads}):

$$E_{ads} = E_C + E_G - E_{C-G} \tag{1}$$

Where E_C, E_G, and E_{C-G} are the energy of the corrole, graphene, and corrole-graphene complexes, respectively, the higher values of E_{ads} stand for the more stable systems. Basis set superposition error (BSSE) were corrected using the counterpoise method [56].

The nature of the intermolecular interactions was explored using the Atoms in Molecules (AIM) analysis, which allows classifying the interaction by the electron density at

the bond critical-point (ρ_{BCP}) of the intermolecular interactions. Under this scope, covalent bonds, coordinate covalent bond/highly polarized interactions, and weak electrostatic interactions are commonly characterized by ρ_{BCP} in the range of ~0.50 - 0.10, 0.10 - 0.04, and ≤ 0.01 e/Bohr^3, respectively. Besides, the reduced gradient method was employed based on the Independent Gradient Model (IGM), which allows differentiation of the intermolecular and intramolecular interactions [57]. The AIM and IGM analyses were carried out using the wavefunction analyzer Multiwfn3.7 program [58].

Magneto-chemical properties were evaluated from broken symmetry solutions for antiferromagnetic (AFM) and ferromagnetic (FM) magnetic states [59]. The electronic structure of the magnetic systems was characterized by the unrestricted corresponding orbitals [60,61], which described the magnetic exchange pathways and the overlap of the corresponding magnetic orbitals. The Heisenberg -Dirac-Van Vleck spin Hamiltonian [62] that described the exchange coupling of **C** and **C-G** systems follows:

$$\hat{H} = -\sum_{1 \geq 2} J_{12}\, \hat{S}_1 \cdot \hat{S}_2 \tag{2}$$

Where H, J_{12}, $\hat{S}_1$, and $\hat{S}_2$ are the spin Hamiltonian, the magnetic coupling constant between fragment 1 and 2, the spin operators for fragment 1, and the spin operator for fragment 2, respectively. The broken-symmetry approach with non-projected spin employed has been extensively used for transition metal complexes [63–67]. The J values were calculated as follows [68,69]

$$J = \frac{E_{HS} - E_{BS}}{\langle S^2 \rangle_{HS} - \langle S^2 \rangle_{BS}} \tag{3}$$

Where E_{HS} and E_{BS}, are the electronic energy of the high spin, broken-symmetry states relative to FM and AFM states, respectively. While $\langle S^2 \rangle_{HS}$, and $\langle S^2 \rangle_{BS}$ are the total spin for high-spin and broken symmetry states, respectively.

Finally, the geometrical distortion (g_d) due to ligand field effects (concerning ideal solids) was characterized using the Shape 2.1 program [70], where the g_d function is obtained as (Eq. 4):

$$g_d = min \frac{\sum_{k=1}^{N}|Q_k-P_k|^2}{\sum_{k=1}^{N}|Q_k-Q_0|^2} \times 100 \tag{4}$$

Thus, the terms g_d can be compared with the ideal polyhedron composed of N vertexes. Q_0, Q_k, and P_k are the mass center, distorted, and perfect vector coordinates, respectively. The boundary conditions are between $100 \geq g_d \geq 0$, where lower limits stand for structures that match the target symmetry, and higher values stand for distorted structures [71].

3. Results and Discussion

The stability of copper corroles/graphene hybrids was examined considering the adsorption energy and the characterization of their intermolecular interaction. Besides, structural properties, reactivity indexes, and frontier molecular orbitals were discussed. Finally, the magneto-chemical characterization based on the broken-symmetry approach described the enhanced magnetic response and the spin transfer.

3.1. Isolated copper corroles and graphene nanosheet as a platform

3.1.1. Stability and structural properties of isolated systems

Firstly, we described the stability of graphene nanosheet and the copper corrole (**CuC**) structures employing energetic values. Thus, the E_{coh} values reach about –7.0 and –

5.4 eV for graphene nanosheet and copper corroles, respectively. Besides, the local interaction of the Cu center with corrole ligands was also examined using the interaction energy (ΔE_{INT} in **Table 1**), i.e., metal-ligand binding energy, demonstrating the strong interactions which rise up to −34.7 eV.

Table 1. Cohesive energy (E_{coh}), interaction energy (ΔE_{INT}), and dihedral angles of copper corroles (CuC). The angles α, β, γ, δ, and ψ are expressed in (º) while E_{coh} and ΔE_{INT} are in eV units.

System	E_{coh}	ΔE_{INT}	α	β	γ	δ	ψ
C1	-5.4	-34.3	11	-13	-20	11	3
C2	-5.3	-33.6	-1	15	-10	-2	8
C3	-5.2	-33.7	-2	13	-5	-4	8
C4	-5.1	-33.5	0	17	-17	0	9
C5	-5.4	-33.5	25	-46	-49	43	0
C6	-5.3	-34.2	1	-10	9	1	-9
C7	-5.3	-33.2	6	-43	22	14	-9
CAHYOB [72]	-	-	-4	4	4	2	-1
IREVAE [73]	-	-	1	2	2	-2	-1
RINCAS [74]	-	-	11	-25	-24	14	4
KAGGIJ [75]	-	-	25	-41	-52	46	5

Secondly, we described the geometrical parameter of the built graphene nanosheet (**G**), specifically C−C bond lengths and ∢CCC angles, which reach average values of 1.4 Å and 120º, respectively (**Fig. 1a**). The CuC showed different lengths varying from 9.3 to 24.3 Å (**Fig. 2a**) regarding the boundary length of the corresponding substituents linked at the *meso* positions of the corrole core. The obtained geometric parameters of **CuN4** core in the isolated copper corroles (**C1-C7**) agree with related reported compounds obtained from theoretical and experimental analyses [41,76,77]. For instance, the average Cu−N bond length of about 1.9 Å, while ∢NCuN axial angles are 80 - 81º and 97 - 98º for ∢N_1CuN_1 and ∢N_2CuN_2, respectively (see **Fig. 2b** for general labeling).
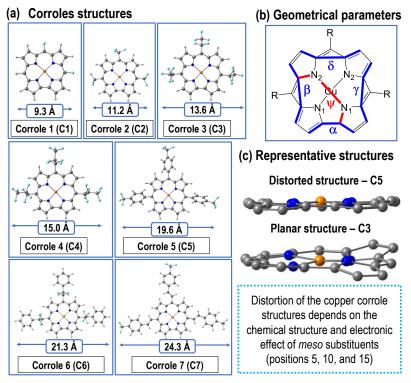
Fig. 2. (a) Molecular length of relaxed geometries for copper macrocycles **C1-C7**. (b) general labeling of the geometrical parameters regarding the core center and dihedral angles representation based on the corrole template. (c) representative cases of distorted and planar copper corrole core structures.

On the other side, considering the non-innocent character of the corrole ligand in this type of complexes, the structure of the corrole core was analyzed based on the torsion angles (α, β, γ, δ, and ψ) to describe the planarity of the corrole macrocycle [25,45,78], which is summarized in **Table 1** and depicted in **Fig. 2b**. Torsional angles with values close to "0" indicate larger planarity of the ring, while higher absolute values of the angles describe the loss of planarity. The more planar corrole structures were **C3** and **C6**, where the larger torsional angle was β, reaching up to 13°; this value agrees with other structures found in literature such as CAHYOB and IREVAE crystal structure [codes of Cambridge Structure Database (CSD)]. Conversely, **C5** and **C7** display the more considerable loss of planarity, showing β torsional angles that reach −46° and −43°, respectively. Similar torsional angles

were observed for KAGGIJ and RINCAS crystal structures (CSD codes) in agreement with **C5** and **C7**, respectively, demonstrating the validity of the obtained structures. Thus, **C3** and **C5** are representative cases, where planarity distortion depends on the chemical and electronic effect of the *meso* substituents, especially for π-conjugated or aryl groups substituents (**Fig. 2c**). Analogous results were obtained for substituted metallo-corroles described in the literature where the values vary because of steric repulsion of substituents and the metal incorporated in the structure [25,78–80]. For instance, it was shown that the planarity of Au corrole suffered significant changes after iodination; nevertheless, more substantial changes were observed after replacing gold with silver or copper [80]. According to structural searches, *meso* substituents are aryl groups; and only a reduced number of reported copper corroles display non-aromatic groups in these positions according to CSD search. This suggest that the hight factibility of synthesize corroles with different aromatic *meso* substituents can be combined with the choice of metal complexed to tune electronic and structural properties in corroles rational design.

3.1.2. Electronic structure and reactivity

Fig. S1 displays the isosurface plots and energies of frontier molecular orbitals (FMOs), including HOMO and LUMO based on open-shell electronic structures (*i.e.,* the α,β spin-orbital functions). As observed, α,β frontier molecular orbitals are located on the corrole core (average value of 93 %), the R substituents at the 5,15-positions contribute more substantially than the 10-position for **C1** and **C7** systems**.** The α-orbitals present a higher HOMO−LUMO gap than the β-orbitals, where the former are 2.2 - 2.7 eV, and the latter is 1.2 - 1.7 eV (α-Δ_{HL}> β-Δ_{HL}, respectively); in both cases, the α,β-Δ_{HL} overcome the 0.8 eV of graphene nanosheet due to the closed-shell nature of this platform (**Fig. S1**). The global Δ_{HL} values are about 1.9-2.1 eV, matching the result with the optical bandgap reported by Agresti

et al.[31]. The same tendency of Δ_{HL} has been observed in other DFT calculations of copper corroles substituted in *meso*-positions [45,76].

Toward a deep understanding of the electronic properties of the studied compounds, global reactivity indexes were also analyzed. **Table 2** also depicts the global indexes considering the chemical potential (μ), molecular hardness (η), and electrophilicity (ω). The maximum hardness principle states that stable systems show resistance to modification on the electron density distribution; *ergo,* higher molecular hardness is expected. Thus, the studied copper corroles display η values of 0.9 - 1.1 eV, suggesting a similar behavior within the studied **CuC** series. The harder system is the fluorinated case (**C1**) due to the direct effect of fluorine atoms (as the harder element) over the **CuC** electron structure. At the same time, the lower η value is found for the alkenyl *meso* substituents (**C7**) attributable to the π-conjugation of R groups with the **CuC** core, in agreement with the observed FMOs for this compound (**Fig. S1**). As observed in the last row of **Table 2**, the graphene nanosheet presents a considerably lower η value of 0.4 eV, which agrees with the most prominent π- conjugation on the whole surface, thus, providing a planar structure with enhanced electronic polarization.

Table 2. Electronic properties. Δ_{HL}, μ, η, and ω are expressed in eV. Multiplicity (2S+1), exchange coupling constant (J), and the overlap (S^2) between corresponding magnetic orbitals. J is in cm^{-1}. g_d is in arbitrary units.

System	Δ_{HL}	μ	η	ω	2S+1	J	$\%S^2$	g_d
C1	2.2	-4.1	1.1	7.6	3	3	3	0.446
C2	1.9	-4.6	1.0	10.7	3	14	1	0.305
C3	2.0	-4.6	1.0	10.7	3	40	0	0.319
C4	2.0	-4.7	1.0	10.8	1	-20	1	0.300
C5	2.1	-4.2	1.0	8.5	1	-1168	25	0.992
C6	2.0	-4.2	1.0	8.8	3	32	0	0.310
C7	1.8	-4.2	0.9	9.8	3	82	1	0.368
G	0.8	-3.7	0.4	18.1	1			

Additionally, μ is related to the electronegativity χ through $\mu = -\chi$; while ω represent the stabilization when the molecular system gains electrons. Hence, μ and ω are related to the relative electrophilic character [55]. With this in mind, the fluorinated alkyl chains in *meso* positions (**C2-C4**) display the more prominent electrophilic character due to the electron-withdrawing effect of these substituents. The electrophilic character is also achieved through π-conjugation in **C7** due to π-conjugation of the trifluoromethylphenyl substituents, which promote the delocalization of electron density through the whole **CuC** core.

3.1.3. Spin density and magnetic properties

Regarding the spin density distribution, the Cu center displays values of 0.6 a.u. in agreement with other works related to the magnetic properties of Cu(II) complexes (showing one unpaired electron) [67,81]. Besides, the spin density surface (**Fig. S1**) is located mainly on the **CuC** core, and the surface shape resembles the $3d_{x^2-y^2}$ orbitals as is proper of Cu(II) center in a square-planar ligand field [41,76]. In this sense, part of spin density is localized onto Cu(II). In contrast, the resting spin density is delocalized along with the corrole core showing a non-innocent and magnetic character.

Because of the non-innocent character of the corrole ligand, multiplicity studies were performed to evaluate the spin state of the minimum energy structures showing different values in each case (**Table 2**). The spin density surfaces are plotted in **Fig. S1** according to minimum energy spin states. A ferromagnetic nature is found in compounds **C1**, **C2**, **C3**, **C6**, and **C7**, which display triplet spin-state (2S+1=3) and positive values of the magnetic exchange constant (*J*), oscillating between 3 to 82 cm^{-1}. Conversely, an antiferromagnetic ground state is found for compounds **C4** and **C5**. Noteworthy is the antiferromagnetic behavior of **C5** since it displays the stronger coupling of -1168 cm^{-1} that agrees with the high

overlap between α and β unrestricted corresponding orbitals (UCOs), reaching 25 % on the whole molecule (**Fig. 3a**). This overlap is allocated on the Cu center, in contrast to the strong ferromagnetic case (**C7**), showing no overlap on the metal center and reaching only 1.25 % of overlapping on the whole molecule (**Fig. 3b**).
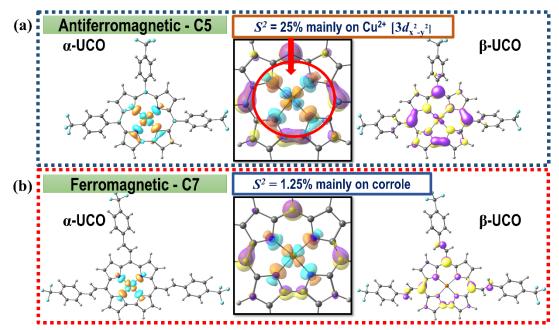

Fig. 3. Representation of unrestricted corresponding magnetic orbital for (a) **C5** antiferromagnetic corrole and (b) **C7** ferromagnetic corrole. Isodensity value of 0.05 a.u. for each surface.

It is necessary to note that the relationship between overlapping magnetic orbitals and the antiferromagnetic nature of the coupling is revisited in Goodenough-Kanamori's model to understand the magnetic behavior of complexes in solid-state [82,83]. Thus, the orthogonality and overlapping between magnetic orbitals are essential descriptors for exploring magnetic properties from a chemical point of view. Nonetheless, other structural parameters also act onto the orbital orthogonality and overlapping, such as planarity of the ring, which can affect the magnetic exchange between corroles, as found in the literature for bis-copper corroles [84]. For this reason, the geometrical distortion (g_d, **Table 2**) of the **CuN4** core was compared to the symmetric square plane structure (point group D$_{4h}$) as a descriptor

of the ligand field influence on the magnetic behavior. Thus, the higher g_d value is found for stronger antiferromagnetic coupling in **C5**, reaching almost the unity. Besides, a statistical study to rationalize the magnetic behavior, structural parameters, and electronic properties demonstrate correlations of magnetic coupling with α, δ, g_d, and S^2, displaying correlation parameters of 0.77, 0.81, 0.95, and 0.99, respectively (**Fig. S2**). Lastly, we highlighted that even the non-innocent character of corroles is strongly dependent on the planarity of corrole, substituent steric effects, and the metal center [85], corroborating the significant influence of structural and chemical modification on the electronic properties of corroles.

3.2. Hybrid materials corroles-graphene

3.2.1. Stability and structural properties of C-G hybrids

Copper corroles are adsorbed in a stacked planar configuration (**Fig. 4**) at distances (d_{stack}) of 3.0 - 3.2 Å and adsorption energy between 2.0 - 3.9 eV (**Table 3**). These results are in agreement with non-metallated corroles adsorbed onto oxidized graphene, where a stacked conformation is more stable (E_{ads} = 1.4 eV) than lateral conformation (E_{ads} = 0.2 eV) [86]. Additionally, the stacked conformation has been corroborated for the corrole adsorption onto metallic surfaces such as Au(111), Ag(111), and Pt(111) [76,87–90]. Remarkably, the non-covalent adsorption of corroles and corrolato onto Ag(111) displayed adsorption energies in the range of 2.8 - 4.7 eV[88]. Furthermore, the π-electron conjugation between radical corroles and the surface increases the stabilization due to aromatic effects [88].
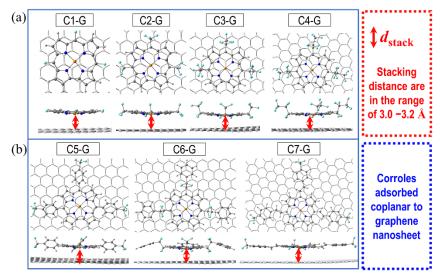
Fig. 4. Relaxed molecular structures of the C-G hybrids (top and side views). (a) Hybrids with non-aromatic substituents and (b) hybrids with aromatic substituents.

The adsorption energy was decomposed in terms of the interaction and preparation energy (ΔE_{INT} and ΔE_{PREP}, respectively) following the expression: $-E_{\text{ads}} = \Delta E_{\text{INT}} + \Delta E_{\text{PREP}}$. Significant correlations were found between E_{ads}, $|\Delta E_{\text{INT}}|$, and the number of carbon atoms in each copper corrole (**Fig. S3**). The adsorption energy per carbon atom (E_{ads}/C) displayed an average value of ~90 meV/atom, indicating that more substantial stabilization will be achieved for larger R substituents. For instance, the lower stabilization is obtained for the **C1-G** hybrid, while the more considerable stabilization for the **C7-G** hybrid. Moreover, ΔE_{PREP} represents the energy penalty due to the deformation of graphene and copper corroles during the adsorption process. Thus, higher deformation is observed in the hybrids with aromatic substituents. This observation can be related to the steric effects in the aromatic R substituents, compared to the non-aromatic fluoroalkyl substituents, where the latter present a lower rotational barrier (similar to alkyl groups) than π-conjugated groups. For instance, the vinyl group rotation in **C7-G** suffers steric impediment between phenyl hydrogen atoms and corrole outer hydrogen atoms, while the C=C double bond cannot rotate freely. Thus, the preparation energy involved in the deformation increases for the aromatic substituents during

16

the stacking process. As an illustration of the structural changes, the torsion angles reflect the increase of planarity of the corrole cores, which can be observed by the decrease of α, β, γ, δ, and ψ angles (**Table 3**). Thus, the increase of planarity is due to electronic interactions with the graphene surface, similarly to the study of copper corroles adsorbed onto Au(111) surface [76] and for non-metallated corroles adsorbed onto Ag(111) surface [88].

Table 3. Electronic properties of **C-G** hybrids. Charges are expressed in |*e*|, while μ, η, ω, and E_{ads} are in eV.

System	d_{stack}	E_{ads}	ΔE_{INT}	ΔE_{PREP}	Q_{CT}	α	β	γ	δ	ψ
C1-G	3.0	2.1	-2.3	0.2	0.0	0	-8	10	-1	-1
C2-G	3.1	2.4	-2.6	0.2	0.6	0	-7	9	0	0
C3-G	3.1	2.0	-2.3	0.3	0.8	0	-5	7	-1	2
C4-G	3.2	2.5	-2.6	0.2	0.8	11	-26	-13	16	0
C5-G	3.2	2.9	-3.6	0.6	0.1	13	-26	-2	3	0
C6-G	3.2	3.0	-3.4	0.4	0.0	1	-13	11	1	-3
C7-G	3.1	3.9	-4.3	0.4	0.0	12	-6	-32	20	4

On the other hand, the charge transfer (Q_{CT}) flows from graphene to the copper corroles, where the higher transference occurs for corroles with non-aromatic fluoroalkyl substituents (**C2-G**, **C3-G,** and **C4-G**) due to a strong electron-withdrawing effect. The highest electron transfer reaches 0.8 |*e*| (copper corroles gain negative charge), indicating that the graphene behaves as an electron reservoir. Conversely, the **C1-G**, **C5-G**, **C6-G**, and **C7-G** hybrids showed almost neglectable charge transfer (Q_{CT}~0|*e*|). In this sense, the electron-withdrawing effect of non-aromatic fluoroalkyl substituents supports the charge movement from graphene; nonetheless, the charge transfer is not the dominant influence on the stabilization mechanism of **C-G** hybrids since no correlation between Q_{CT} and E_{ads} is observed (**Table 3**).

In this regard, we have explored the nature of chemical bonds using the AIM method to detect specific interactions between both components. However, the extended number of

intermolecular interactions present values of ρ_{BCP} in the range of $0.001 - 0.013$ $|e/\text{Bohr}^3|$, indicating that the very weak electrostatic interactions that contribute to the stabilization. Nonetheless, the interaction mechanism in **C-G** hybrids should be driven by Van der Waals forces derived from π-conjugation of corroles interacting with graphene in a parallel displaced π- stacking. With this in mind, the non-covalent interactions were explored using the independent gradient model to characterize the dispersive driving force pictorially (**Fig. S4** and **Fig. 5**). The regions of strong stabilization [red colored for sign(λ_2)ρ negative values] are mainly located below fluorine, and H-π interactions form stabilizing interactions, while subtle stabilizing regions are located below copper and nitrogen atoms that belong to **CuN$_4$** core (**Fig. 5**). Conversely, repulsive interactions [blue colored for sign(λ_2)ρ positive values] between Cu−N bonds and graphene are observed, and especially the most intense steric repulsion is observed between twisted phenyl group and graphene nanosheet in **C5-G** hybrid. Considering IGM surfaces size, there is some correspondence with the E_{ads} tendency since **C5-G, C6-G,** and **C7-G** hybrids are the more stable systems. The latter can be explained considering that the sum of an extended number of low stabilizing interactions achieves a valuable contribution to the whole stabilization. This point suggests that the dispersion forces are presumably the driving forces for the interaction of **C-G** hybrids, considering the π-stacking prevalence in all the current studied hybrids.
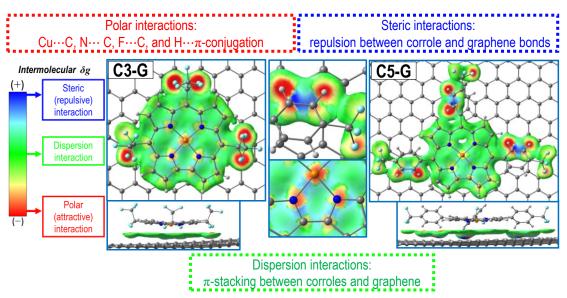
Fig. 5. Molecular isosurfaces based on intermolecular IGM for C-G hybrids. δg^{inter}=0.005 a.u., color coding in the electron density range $+0.025 > sign(\lambda_2)\rho > -0.025$ a.u. (map region in blue and red color, respectively)

3.2.2. Electronic structure and reactivity of C-G hybrids

The electronic structure of **C-G** hybrids is revised regarding the FMOs surfaces for α,β-frontier molecular spin-orbitals, and the global reactivity descriptors (**Fig. S5** and **Table 4**). In the C-G hybrids, the copper corroles participate more actively for the α,β frontier molecular spin-orbitals, in contrast with the isolated copper corroles. This kind of distribution has been reported previously for the adsorption studies of 2D nanomaterial [91]. Indeed, four different cases are observed for the α,β-Δ_{HL} depending on the corroles participation:

1) the HOMO/LUMO pair located both onto graphene [HOMO(G)/LUMO(G)] displaying HOMO-LUMO gaps of 0.7 - 1.2 eV;

2) the HOMO/LUMO pair is distributed onto copper corroles [HOMO(C)/LUMO(C)] display a value of 0.3 eV, *e.g.,* α-HOMO(C2)/LUMO(C2);

3) the HOMO(G)/LUMO(C) pair showing α,β-Δ_{HL} values of 0.5 - 0.7 eV.;

4) the HOMO(C)/LUMO(G) pair presenting the low gaps between 0.1 - 0.3 eV.

For instance, **C3-G** hybrids can be classified as *case-4*, displaying low global Δ_{HL} with values of 0.1 eV. In contrast, the **C5-G** hybrid is a mixture of *case-1* and *case-3*, reaching up to 0.9 eV, close to the isolated graphene nanosheet (Δ_{HL}=0.8 eV, **Table 2**) in correspondence with a significant contribution to the α and β spin-orbitals.

Table 4. Electronic properties of C-G hybrids. Δ_{HL}, μ, η, and ω are expressed in eV.

System	Δ_{HL}	μ	η	ω
C1-G	0.7	-3.7	0.4	19
C2-G	0.5	-3.9	0.2	31
C3-G	0.1	-3.8	0.1	123
C4-G	0.2	-3.8	0.1	59
C5-G	0.9	-3.8	0.5	16
C6-G	0.6	-3.8	0.3	23
C7-G	0.7	-3.7	0.3	21

Comparatively, the reactivity is in line with the participation of the fragment involved in frontier molecular spin-orbitals. For instance, **C1-G**, **C5-G**, **C6-G,** and **C7-G** hybrids present close to 75 % of graphene participation in the Frontier Molecular Orbitals, preserving graphene's reactivity descriptors (μ = −3.7 eV, η = 0.4 eV, and ω = 18.1 eV). On the other hand, for **C2-G**, **C3-G,** and **C4-G** hybrids, the corrole moiety introduces orbitals between graphene frontier molecular orbitals decreasing the Δ_{HL} and η, while ω increases substantially. Considering the relation between Δ_{HL} with optic and conducting properties, the *case-3* and *case-4* outstand by the opportunity of the generation electron mobility employing light stimuli. For example, in the *case-3*, light can promote electron density from G to CuC employing only ~1700 nm (0.7 eV according to results). While the *case-4* displays the lowest values of Δ_{HL} suggesting a conductor behavior between **G** and **CuC** pair. Both cases Thus, the results suggest a wide versatility of **CuC** developing chemical modification of the substituents as an invitation to evaluate the optic, conduction, and sensing applications.

From a structural point of view, changes in planarity substantially affect the orbital structure of metallo-macrocycles. Because of their planar structure, the orbitals of copper are orthogonal to the π-conjugation of corrole, favoring the formation of d-π hybrid orbitals. Besides, the increase of planarity supports the π−π stacking with graphene-based surfaces [92]. The frontier molecular spin-orbitals are affected in similar corroles adsorbed onto Au(111), Ag(111) and Cu(111) surfaces [76,88,89,93]. These changes could be observed experimentally using scanning tunneling microscopy (STM) and Kondo resonance; nevertheless, the main effects are linked to magnetic properties.

3.2.3. Magneto-chemical properties

Regarding the magnetic properties of the **C-G** hybrids, the unpaired electrons can be distributed within the whole system, including the graphene platform. Indeed, the spin density surface of **C-G** hybrids is mainly allocated on both copper corroles and the edge of the graphene nanosheet (**Fig. S5**). Indeed, spin density delocalization/polarization mechanism is present in all the cases that agree with other studies, especially for graphene nanoribbons indicating that electronic structure is in line with experimental evidence [94,95]. On the other side, it is essential to differentiate the charge transfer (Q_{CT}) vs. spin-transfer phenomena since the spin density (ρ_S) is the difference between α and β spin density: $\rho_S = \rho_\alpha - \rho_\beta$. In this sense, the Q_{CT} parameter does not differ between α and β electrons, but spin density transfer can occur with $Q_{CT} = 0$ if the spin density location is balanced [76,96]. In the cases of **C2-G**, **C3-G**, and **C4-G** hybrids, charge transfer/spin density delocalization coincides, analogous to forming a transient corrole radical due to an electron transfer [88]. Ag(111) surface transfers electron and spin density to corrole due to dispersion and aromatic

driving forces. In this sense, the aromatic character of the fragment of the **C-G** hybrid arises as other stimuli to reach higher magnetic coupling.

Since the spin density is allocated on graphene, this effect modified the magnetic behavior substantially. The spin-transfer occurs on graphene by the interaction with corroles. By analogy with Q_{CT}, the spin-transfer (ρ_{ST}) can be quantified summing the atomic spin density of each atom that compose a fragment. In this sense, the ρ_{ST} of the graphene fragment will reveal how corroles can generate a magnetic response over the platform. The ρ_{ST} values suggest that an integer spin is transferred to graphene (**Fig. 6a**). For instance, no spin-density is transferred for **C1-G,** and **C6-G** hybrids; close to one spin was transferred for **C2-G**, **C3-G**, **C4-G**, and **C5-G** hybrids, while two spins were transferred to **C7-G** hybrid. Because of the π-conjugated character of graphene, the spin density is delocalized along the nanosheet, but a directional spin polarization is observed, especially for the ferromagnetic hybrids (**Fig. 6b** and **Fig. S5**). Interestingly, correlations were observed when comparing the geometrical distortion of **CuN₄** core (g_d) with spin transfer (**Fig. S6**). Besides, the stability descriptors are also related to spin-transfer since electronic hardness (kinetic stability), and adsorption energy (thermodynamic stability) show significant correlation parameters (**Fig. S6**). These results suggest that the spin transfer process is associated with the structural and electronic properties of the copper corroles, indicating that spin transfer to graphene is a complex process that involves several variables.
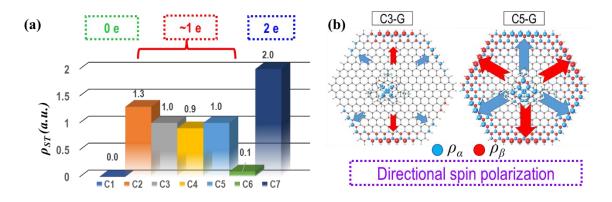
Fig. 6. (a) Spin transfer for C-G hybrids. (b) spin density surface for **C3-G** and **C5-G** hybrids. Isodensity value of 0.003 a.u. for each surface.

On the other hand, the magnetic response of most systems increases in terms of the absolute value, being the ferromagnetic nature more strongly favored. The **C5-G** hybrid shows the stronger ferromagnetic coupling of +3316 cm^{-1} with no overlap between corresponding magnetic orbitals (**Table 5**). The strong ferromagnetism agrees with the low overlap between magnetic orbitals and the increase of planarity for copper corroles since the planarity of the corrole ligand supports the π-conjugation where the orbitals are orthogonal to the $3d_{x2-y2}$ proper of Cu(II) centers stabilizing the ferromagnetic states. Conversely, the **C3-G** hybrid displays a more robust antiferromagnetic behavior with −1869 cm^{-1} and a high % S^2 of magnetic orbitals reaching up to 63 %. Comparatively, a set of copper corroles adsorbed on Au(111) reported magnetic couplings between −909 to +1784 cm^{-1}, suggesting that the magnetic properties of copper corroles are highly modulable by the incorporation of new substituents [76]. These magnetic behaviors were reported for silver corroles where π-conjugation also interacts with the $4d_{x2-y2}$ orbital of Ag(II), but the higher torsional angles in the distorted structure obstruct the ferromagnetic coupling. Consistently, a previous study reports the strong antiferromagnetic coupling of non-metalated corroles adsorbed onto Ag(111), reaching up to −2371 cm^{-1} [89].

Table 5. Magnetic properties of **C-G** hybrids and copper corroles employing the hybrid geometry (C*). Multiplicity (2S+1), exchange coupling constant (J), and the overlap (S^2) between corresponding magnetic orbitals. J is expressed in cm^{-1}.

System	2S+1	J	$\%S^2$	System	2S*+1	J*	$\%S^{*2}$	ΔS	ΔJ
C1-G	3	1267	0	C1*	3	214	0	0	1053
C2-G	3	2003	1	C2*	3	1168	0	0	835
C3-G	1	-1869	63	C3*	1	-364	0	0	-1505
C4-G	3	1470	8	C4*	3	883	1	0	587
C5-G	3	3316	0	C5*	3	100	0	0	3216
C6-G	3	13	0	C6*	3	14	1	0	1
C7-G	3	824	3	C7*	1	-106	4	1	940

The characterization of corresponding magnetic orbitals evidences the exchange pathway between the magnetic centers. In fact, the **C5-G** hybrid outstands by the substantial magnetic response due to the high stabilization of the high-spin state (triplet state) and its consequent null overlap between α,β-UCOs. Indeed, the surface of α-UCO is allocated onto corroles while β-UCO is distributed on graphene lacking contact between both magnetic orbitals (**Fig. 7a**), and the unpaired electrons cannot interact by a direct magnetic pathway. On the contrary, the **C3-G** hybrid displays strong antiferromagnetism due to the high α,β-UCOs overlap (63 %), which occurs on graphene and not on the C-G hybrids (**Fig. 7b**). Indeed, the unpaired electrons can interact antiferromagnetically through the exchange pathway with no resistance. Considering the current evidence, the graphene nanosheet is presented as a platform able to act as an amplifier of the magnetic response that directs/conducts the spin transfer through its structure.
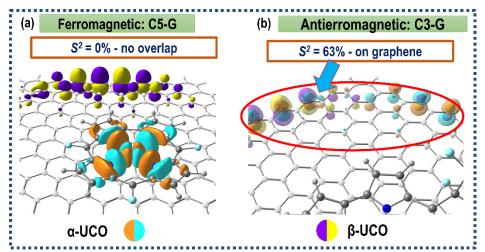
Fig. 7. Representation of unrestricted corresponding magnetic orbital for (a) **C5-G** hybrid and (b) **C3-G** hybrid. Isodensity value of 0.025 a.u. for each surface.

However, it is necessary to decipher if the current magnetic behavior is part of structural changes, spin-transfer phenomenon, or this behavior results from the synergistic effect between the properties mentioned above. With this purpose, the magnetic properties of copper corroles retaining the geometry of **C-G** hybrids were evaluated and marked with the "*" symbol. Besides, the change in the coupling constant (ΔJ) and magnetic moment variation (ΔS) were calculated as follow: $\Delta J = J\text{-}J^*$; $\Delta S = S\text{-}S^*$ (**Table 5**). These descriptors are addressed to evaluate the effect of the interaction between graphene nanosheet and the **CuC**. For example, if $\Delta S=0$, no magnetic reversion occurs, while $\Delta S=1$ indicates a reversion of the magnetic nature. Moreover, if $\Delta J = 0$, no magnetic changes occur; $\Delta J > 0$ implies a ferromagnetic contribution, and $\Delta J < 0$ reveals antiferromagnetic contribution due to the interaction with graphene nanosheet. With this in mind, the magnetic properties of copper corroles showed a ferromagnetic contribution of graphene for **C1-G**, **C2-G**, **C4-G**, **C5-G,** and **C7-G** hybrids, suggesting an amplification of the magnetic response rising to $\Delta J = 3216$ cm^{-1}. Whereas the **C3-G** hybrid presented an antiferromagnetic contribution of -1505 cm^{-1}, the **C6-G** hybrid is almost not affected by the interaction with graphene. Lastly, the reversion of the magnetic nature only occurs in **C7-G** since this hybrid becomes ferromagnetic due to

25

the interaction with graphene. Therefore, the graphene nanosheet can affect the magnetic response in two ways: (i) affecting the structural array during the adsorption process and inducing planarity to copper corroles; (ii) offering an electronic platform to amplify the magnetic response by spin transfer. Thus, graphene actively stabilizes the hybrids and modifies the structural, electronic, and magnetic properties of **C-G** hybrids.

The magnetic properties were compared with structural and electronic properties to get a deeper insight into **C-G** hybrids. Hence, the statistical analysis of these properties allows us to determine the most important variables through correlation analysis. For instance, a strong correlation between the electrophilicity and the overlap of corresponding magnetic orbitals (S vs. ω plot in **Fig. S7**) suggests that a more considerable overlap supports the stabilization of additional electron density. Even more, following this line of analysis, the correlation between ΔJ and ω demonstrate that high electrophilic **C-G** hybrids support the augmented antiferromagnetic response (ω vs. ΔJ plot in **Fig. S7**). That is why the **C3-G** hybrid presents the augmented antiferromagnetic response after adsorption. Furthermore, similar analysis indicates that the geometrical distortion of the **CuN₄** (in isolated copper corroles) and its variation concerning **C-G** hybrids (g_d and Δg_d, respectively) is involved in the augmented magnetic response due to graphene interaction (plots relative to ΔJ in **Fig. S7**). In consequence, the explanation of the augmented magnetic response of **C-G** hybrids is consistent with the magneto-chemistry either by analyzing the chemical structure, the electronic properties, the corresponding magnetic orbitals, and the respective hybrid stabilization during the adsorption process.

3.3. Outlook for technological applications

This work provides a conceptual perspective for exploring the stability, electronic properties, and magnetic response of copper corroles deposited onto a graphene surface.

Moreover, the discussed results provide a consistent basis for future theoretical/experimental studies on corrole/graphene hybrids. Regarding the applicability of metallo-corroles in catalysis, molecular electronics, sensing, optics, and spintronics, the understanding of their properties is a prominent challenge that should support the rational design of the material. Besides, experimental studies have supported the use of graphene for spintronics due to attractive advantages in spin transport measurements compared to metals and semiconductors. For instance, graphene presents favorable physical characteristics at room temperature [97–99], such as longer spin lifetimes, larger spin signal, and longer spin diffusion lengths than copper, aluminum, silver, and highly doped silicon [100–105]. On the other side, spin-injection and spin-transport in graphene are crucial for designing new magnetic devices, especially if it is considered the strongly diamagnetic behavior as pristine nanosheets. However, cooperative magnetic ordering can be introduced to graphene as a result of vacancy defects, incorporation of light adatoms (hydrogen and fluoride), incorporation of heavy adatoms, substitutional doping using light or heavy atoms, molecular doping, and coupling to a ferromagnetic substrate. Thus, the induction of magnetic moment in graphene is a prominent goal toward developing spin logic devices [106–109].

Eventually, graphene would substitute the conventional ferromagnetic thin films since single-atomic permanent ferromagnets are more scalable than thin films with thicknesses of less than 200 nm, which present the desired changes in magnetic properties such as more significant magnetic anisotropy and dynamic magnetic response a. In addition, experimental evidence demonstrates graphene as a versatile platform for spintronic application due to the ability to turn on/off the Kondo effect by electrical control, adsorption magnetic molecules [113]. Kondo resonance signals are associated with the magnetic coupling between the unpaired spins of the paramagnetic molecules and the conduction band electrons of the metal

substrate. Thus, when a little portion of paramagnets is deposited on a conductive material (metals, graphene, carbon quantum dots, among others), at low temperature, some electric resistance deviation occurs because of the mentioned magnetic coupling [114]. Regarding the applicability of **C-G** hybrids, the ferromagnetic coupling is desired since the system displays the spin oriented in the same direction, which allows to univocally interact with an electric current in spin valves or other spintronic devices. In this sense, the enhanced magnetic response for ferromagnetic hybrids is the desired condition for future magnetic application. Besides, the intermolecular interactions of the **C-G** hybrid suggest that spin transfer to graphene platform is directionally polarized to the nanosheet edges. Henceforth, graphene incorporates an active magnetic nature without losing the chemical integrity, unlike other strategies to get magnetization such as vacancy defects, substitutionally or adatom doping, or chemical reactions to couple a ferromagnet [106,107]. Clearly, the molecular deposition or adsorption process involves milder conditions that mainly support the desired magnetic behavior preserving the structural integrity of the systems.

Finally, the improvement in magnetic devices not only point to miniaturizing but rather to energy efficiency, decrease energy consumption, reduction of heat dissipation, while increasing information capabilities can be achieved [110]. In this sense, the overcoming of the challenge of generate new devices at the technological limits, increase the efficiency, increase the computing capabilities, decrease the energy demand, and help environment. Thus, the augmented ferromagnetic response allow to orient the spins applying a external field while the orientation is more resistant to thermal disordering [111] enhancing the info writing process (**Fig. 8a**). Moreover, the non-innocent character of the ligand may and the tunable conductivity in the hybrid complex suggest a high sensitivity to any perturbation. In effect, copper porphyrins and copper phthalocyanines have been used to detect gases such

as ammonia and nitrogen oxide [112] but it is expected that non-innocent character of corroles support the sensing since a wide area is sensible to any perturbation (**Fig. 8b**). Besides, the tunability of the frontier molecular orbital gap suggest that conductivity can be tuned to enhance the electronic communication for corrole-based hybrid materials. Therefore, the study of copper corroles-graphene hybrids is not only a prominent challenge rather also a rich field for the development of new magnetic, sensing, and optical applications.

Fig. 8. Schematic representation for potential technological applications of copper corroles hybrid material for (a) spintronic devices (b) gas sensing.

4. Concluding remarks.

In summary, a series of non-covalent hybrid systems based on fluorinated A_3-type copper corrole complexes adsorbed on a pristine graphene sheet was studied by DFT calculation. A magneto-chemical point of view allows stating the main variables that control the stability of the **C-G** hybrids, unraveling the influence of electronic structure in the magnetic properties of the studied hybrids. The results showed that the hybrids display significant stabilization with adsorption energies in the range of 2.0 to 3.9 eV. This stabilization is favored by a π-π stacking with distances about 3.1 Å between both fragments, where graphene behaves as an electron reservoir for the most conductive cases. At the same time, isolated copper corroles showed characteristic geometrical deformations, mainly due to the non-innocent nature of the ligand. A significant flattening corrole ligand accompanies the

formation of the corresponding hybrid. Summarizing (i) the geometrical rearrangement of the corroles during the adsorption onto graphene could be induced by weak electrostatic interactions and dispersion forces, (ii) *meso*-substituents affect the electronic properties of the hybrids, especially kinetic stability based on the electronic hardness of the corresponding systems. (iii) Graphene modulated the reactivity of the hybrid systems displaying active participation on the HOMO and LUMO; the lowest reactivity was observed to hybrids with a more significant contribution of G on the frontier molecular orbitals. (iv) The geometrical distortion of the copper corroles directly impacted the magnetic response since it correlated the ligand field distortion and the overlapping of the corresponding magnetic orbitals. (v) Finally, the exposed results suggest that aryl-substituted corroles at the *meso* positions support the augmented magnetic response of the hybrid system, while electrophilicity of hybrids acts to the detriment of the ferromagnetic coupling. Statistical correlation analysis supported the rationalization of the augmented magnetic response and the spin transfer phenomena, indicating that spin transfer is related to kinetic and thermodynamic stability. Under the same scope, the geometrical distortion of the **CuN_4** core was associated with the spin transfer and the magnetic response, which is consistent with the well-known influence of the ligand field for transition metal complexes.

Acknowledgements

There are no competing interests to declare by the authors of this article.

Reference

[1] H. Wang, L. Wang, F.-S. Xiao, Metal@Zeolite Hybrid Materials for Catalysis, ACS Cent. Sci. 6 (2020) 1685–1697. https://doi.org/10.1021/acscentsci.0c01130.

[2] F. Limosani, F. Tessore, G. Di Carlo, A. Forni, P. Tagliatesta, Nonlinear Optical Properties of Porphyrin, Fullerene and Ferrocene Hybrid Materials, Materials (Basel). 14 (2021) 4404. https://doi.org/10.3390/ma14164404.

[3] M. Adnan, J.J. Baumberg, G. Vijaya Prakash, Linear and nonlinear optical probing of various excitons in 2D inorganic-organic hybrid structures, Sci. Rep. 10 (2020) 2615. https://doi.org/10.1038/s41598-020-59457-7.

[4] S.A. Didas, S. Choi, W. Chaikittisilp, C.W. Jones, Amine–Oxide Hybrid Materials for CO_2 Capture from Ambient Air, Acc. Chem. Res. 48 (2015) 2680–2687. https://doi.org/10.1021/acs.accounts.5b00284.

[5] J. Chu, P. Shi, W. Yan, J. Fu, Z. Yang, C. He, X. Deng, H. Liu, PEGylated graphene oxide-mediated quercetin-modified collagen hybrid scaffold for enhancement of MSCs differentiation potential and diabetic wound healing, Nanoscale. 10 (2018) 9547–9560. https://doi.org/10.1039/C8NR02538J.

[6] W. Zuo, R. Li, C. Zhou, Y. Li, J. Xia, J. Liu, Battery-Supercapacitor Hybrid Devices: Recent Progress and Future Prospects, Adv. Sci. 4 (2017) 1–21. https://doi.org/10.1002/advs.201600539.

[7] G. Kickelbick, ed., Hybrid Materials, Wiley, 2006. https://doi.org/10.1002/9783527610495.

[8] F. Bonaccorso, L. Colombo, G. Yu, M. Stoller, V. Tozzini, A.C. Ferrari, R.S. Ruoff, V. Pellegrini, Graphene, related two-dimensional crystals, and hybrid systems for energy conversion and storage, Science (80). 347 (2015) 1246501. https://doi.org/10.1126/science.1246501.

[9] G. Bottari, M.Á. Herranz, L. Wibmer, M. Volland, L. Rodríguez-Pérez, D.M. Guldi, A. Hirsch, N. Martín, F. D'Souza, T. Torres, Chemical functionalization and

characterization of graphene-based materials, Chem. Soc. Rev. 46 (2017) 4464–4500. https://doi.org/10.1039/C7CS00229G.

[10]   C.-B. Huang, S. Witomska, A. Aliprandi, M.-A. Stoeckel, M. Bonini, A. Ciesielski, P. Samorì, Molecule-Graphene Hybrid Materials with Tunable Mechanoresponse: Highly Sensitive Pressure Sensors for Health Monitoring, Adv. Mater. 31 (2019) 1804600. https://doi.org/10.1002/adma.201804600.

[11]   Y. Xu, Z. Liu, X. Zhang, Y. Wang, J. Tian, Y. Huang, Y. Ma, X. Zhang, Y. Chen, A Graphene Hybrid Material Covalently Functionalized with Porphyrin: Synthesis and Optical Limiting Property, Adv. Mater. 21 (2009) 1275–1279. https://doi.org/10.1002/adma.200801617.

[12]   S. Yang, Y. Lin, X. Song, P. Zhang, L. Gao, Covalently Coupled Ultrafine H-TiO$_2$ Nanocrystals/Nitrogen-Doped Graphene Hybrid Materials for High-Performance Supercapacitor, ACS Appl. Mater. Interfaces. 7 (2015) 17884–17892. https://doi.org/10.1021/acsami.5b04368.

[13]   A. Wang, L. Long, W. Zhao, Y. Song, M.G. Humphrey, M.P. Cifuentes, X. Wu, Y. Fu, D. Zhang, X. Li, C. Zhang, Increased optical nonlinearities of graphene nanohybrids covalently functionalized by axially-coordinated porphyrins, Carbon N. Y. 53 (2013) 327–338. https://doi.org/10.1016/j.carbon.2012.11.019.

[14]   D. Dasler, R.A. Schäfer, M.B. Minameyer, J.F. Hitzenberger, F. Hauke, T. Drewello, A. Hirsch, Direct Covalent Coupling of Porphyrins to Graphene, J. Am. Chem. Soc. 139 (2017) 11760–11765. https://doi.org/10.1021/jacs.7b04122.

[15]   I. Kruusenberg, J. Mondal, L. Matisen, V. Sammelselg, K. Tammeveski, Oxygen reduction on graphene-supported MN$_4$ macrocycles in alkaline media, Electrochem. Commun. 33 (2013) 18–22. https://doi.org/10.1016/j.elecom.2013.04.005.

[16]   Q. Lu, Y. Zhang, S. Liu, Graphene quantum dots enhanced photocatalytic activity of zinc porphyrin toward the degradation of methylene blue under visible-light irradiation, J. Mater. Chem. A. 3 (2015) 8552–8558. https://doi.org/10.1039/C5TA00525F.

[17]   B.-P. Jiang, L.-F. Hu, D.-J. Wang, S.-C. Ji, X.-C. Shen, H. Liang, Graphene loading water-soluble phthalocyanine for dual-modality photothermal/photodynamic therapy via a one-step method, J. Mater. Chem. B. 2 (2014) 7141–7148. https://doi.org/10.1039/C4TB01038H.

[18]   E. Gacka, A. Wojcik, M. Mazurkiewicz-Pawlicka, A. Malolepszy, L. Stobiński, A. Kubas, G.L. Hug, B. Marciniak, A. Lewandowska-Andralojc, Noncovalent Porphyrin–Graphene Oxide Nanohybrids: The pH-Dependent Behavior, J. Phys. Chem. C. 123 (2019) 3368–3380. https://doi.org/10.1021/acs.jpcc.8b11374.

[19]   E. Gacka, G. Burdzinski, B. Marciniak, A. Kubas, A. Lewandowska-Andralojc, Interaction of light with a non-covalent zinc porphyrin–graphene oxide nanohybrid, Phys. Chem. Chem. Phys. 22 (2020) 13456–13466. https://doi.org/10.1039/D0CP02545C.

[20]   T. Ding, E.A. Alemán, D.A. Modarelli, C.J. Ziegler, Photophysical Properties of a Series of Free-Base Corroles, J. Phys. Chem. A. 109 (2005) 7411–7417. https://doi.org/10.1021/jp052047i.

[21]   G. Lu, W. Lin, Y. Fang, W. Zhu, X. Ji, Z. Ou, Synthesis and electrochemical properties of meso -phenyl substituted copper corroles: Solvent effect on copper oxidation state, J. Porphyr. Phthalocyanines. 15 (2011) 1265–1274. https://doi.org/10.1142/S1088424611004208.

[22]   Y. Fang, Z. Ou, K.M. Kadish, Electrochemistry of Corroles in Nonaqueous Media, Chem. Rev. 117 (2017) 3377–3419. https://doi.org/10.1021/acs.chemrev.6b00546.

[23]   J.F.B. Barata, M.G.P.M.S. Neves, M.A.F. Faustino, A.C. Tomé, J.A.S. Cavaleiro, Strategies for Corrole Functionalization, Chem. Rev. 117 (2017) 3192–3253. https://doi.org/10.1021/acs.chemrev.6b00476.

[24]   L.-G. Liu, Y.-M. Sun, Z.-Y. Liu, Y.-H. Liao, L. Zeng, Y. Ye, H.-Y. Liu, Halogenated Gallium Corroles:DNA Interaction and Photodynamic Antitumor Activity, Inorg. Chem. 60 (2021) 2234–2245. https://doi.org/10.1021/acs.inorgchem.0c03016.

[25]   R.F. Einrem, A.B. Alemayehu, S.M. Borisov, A. Ghosh, O.A. Gederaas, Amphiphilic Rhenium-Oxo Corroles as a New Class of Sensitizers for Photodynamic Therapy, ACS Omega. 5 (2020) 10596–10601. https://doi.org/10.1021/acsomega.0c01090.

[26]   R.D. Teo, J.Y. Hwang, J. Termini, Z. Gross, H.B. Gray, Fighting Cancer with Corroles, Chem. Rev. 117 (2017) 2711–2729. https://doi.org/10.1021/acs.chemrev.6b00400.

[27]   J.-M. Barbe, G. Canard, S. Brandès, R. Guilard, Selective Chemisorption of Carbon Monoxide by Organic–Inorganic Hybrid Materials Incorporating Cobalt(III) Corroles as Sensing Components, Chem. - A Eur. J. 13 (2007) 2118–2129. https://doi.org/10.1002/chem.200601143.

[28]   Y.-J. Lin, W.-Z. Cao, T. Ou Yang, C.-H. Feng, C.-T. Chang, Deciphering the effect of citric acid on arsenic adsorption with phosphorene in aqueous solution, Sustain. Environ. Res. 29 (2019) 22. https://doi.org/10.1186/s42834-019-0021-8.

[29]   F. Cai, F. Xia, Y. Guo, W. Zhu, B. Fu, X. Liang, S. Wang, Z. Cai, H. Xu, "Off–on–off" type of selectively pH-sensing 8-hydroxyquinoline-substituted gallium(III) corrole, New J. Chem. 43 (2019) 18012–18017. https://doi.org/10.1039/C9NJ04544A.

[30]   A. Agresti, B. Berionni Berna, S. Pescetelli, A. Catini, F. Menchini, C. Di Natale, R. Paolesse, A. Di Carlo, Copper-Based Corrole as Thermally Stable Hole Transporting Material for Perovskite Photovoltaics, Adv. Funct. Mater. 30 (2020) 2003790. https://doi.org/10.1002/adfm.202003790.

[31]   B. Mondal, K. Sengupta, A. Rana, A. Mahammed, M. Botoshansky, S.G. Dey, Z. Gross, A. Dey, Cobalt Corrole Catalyst for Efficient Hydrogen Evolution Reaction from H_2O under Ambient Conditions: Reactivity, Spectroscopy, and Density Functional Theory Calculations, Inorg. Chem. 52 (2013) 3381–3387. https://doi.org/10.1021/ic4000473.

[32]   H. Lei, C. Liu, Z. Wang, Z. Zhang, M. Zhang, X. Chang, W. Zhang, R. Cao, Noncovalent Immobilization of a Pyrene-Modified Cobalt Corrole on Carbon Supports for Enhanced Electrocatalytic Oxygen Reduction and Oxygen Evolution in Aqueous Solutions, ACS Catal. 6 (2016) 6429–6437. https://doi.org/10.1021/acscatal.6b01579.

[33]   K. Sudhakar, A. Mahammed, Q.-C. Chen, N. Fridman, B. Tumanskii, Z. Gross, Copper Complexes of CF 3 -Substituted Corroles for Affecting Redox Potentials and Electrocatalysis, ACS Appl. Energy Mater. 3 (2020) 2828–2836. https://doi.org/10.1021/acsaem.9b02465.

[34]   S. Nardis, D. Monti, R. Paolesse, Novel aspects of corrole chemistry, Mini. Rev. Org. Chem. 2 (2005) 355–374.

[35]   R. Orłowski, D. Gryko, D.T. Gryko, Synthesis of Corroles and Their Heteroanalogs, Chem. Rev. 117 (2017) 3102–3137. https://doi.org/10.1021/acs.chemrev.6b00434.

[36]   D.T. Gryko, Adventures in the synthesis of meso -substituted corroles, J. Porphyr. Phthalocyanines. 12 (2008) 906–917. https://doi.org/10.1142/S1088424608000297.

[37] G. Canard, D. Gao, A. D'Aléo, M. Giorgi, F.-X. Dang, T.S. Balaban, meso -Ester Corroles, Chem. - A Eur. J. 21 (2015) 7760–7771. https://doi.org/10.1002/chem.201406369.

[38] S. Ye, T. Tuttle, E. Bill, L. Simkhovich, Z. Gross, W. Thiel, F. Neese, The Electronic Structure of Iron Corroles: A Combined Experimental and Quantum Chemical Study, Chem. - A Eur. J. 14 (2008) 10839–10851. https://doi.org/10.1002/chem.200801265.

[39] H.-K. Norheim, J. Capar, R.F. Einrem, K.J. Gagnon, C.M. Beavers, H. Vazquez-Lima, A. Ghosh, Ligand noninnocence in FeNO corroles: insights from β-octabromocorrole complexes, Dalt. Trans. 45 (2016) 681–689. https://doi.org/10.1039/C5DT03947A.

[40] A.B. Alemayehu, E. Gonzalez, L.K. Hansen, A. Ghosh, Copper Corroles Are Inherently Saddled, Inorg. Chem. 48 (2009) 7794–7799. https://doi.org/10.1021/ic900744v.

[41] C.M. Lemon, M. Huynh, A.G. Maher, B.L. Anderson, E.D. Bloch, D.C. Powers, D.G. Nocera, Electronic Structure of Copper Corroles, Angew. Chemie. 128 (2016) 2216–2220. https://doi.org/10.1002/ange.201509099.

[42] I.M. DiMucci, J.T. Lukens, S. Chatterjee, K.M. Carsch, C.J. Titus, S.J. Lee, D. Nordlund, T.A. Betley, S.N. MacMillan, K.M. Lancaster, The Myth of d8 Copper(III), J. Am. Chem. Soc. 141 (2019) 18508–18520. https://doi.org/10.1021/jacs.9b09016.

[43] K. Pierloot, H. Zhao, S. Vancoillie, Copper Corroles: the Question of Noninnocence, Inorg. Chem. 49 (2010) 10316–10329. https://doi.org/10.1021/ic100866z.

[44] W. Kaim, B. Schwederski, Non-innocent ligands in bioinorganic chemistry—An overview, Coord. Chem. Rev. 254 (2010) 1580–1588. https://doi.org/10.1016/j.ccr.2010.01.009.

[45] Y.K. Maurya, K. Noda, K. Yamasumi, S. Mori, T. Uchiyama, K. Kamitani, T. Hirai, K. Ninomiya, M. Nishibori, Y. Hori, Y. Shiota, K. Yoshizawa, M. Ishida, H. Furuta, Ground-State Copper(III) Stabilized by N-Confused/N-Linked Corroles: Synthesis, Characterization, and Redox Reactivity, J. Am. Chem. Soc. 140 (2018) 6883–6892. https://doi.org/10.1021/jacs.8b01876.

[46] M. Kosa, N. Levy, L. Elbaz, D.T. Major, Theoretical Study of the Electrocatalytic Reduction of Oxygen by Metallocorroles, J. Phys. Chem. C. 122 (2018) 17686–17694. https://doi.org/10.1021/acs.jpcc.8b05831.

[47] X. Li, H. Lei, X. Guo, X. Zhao, S. Ding, X. Gao, W. Zhang, R. Cao, Graphene-Supported Pyrene-Modified Cobalt Corrole with Axial Triphenylphosphine for Enhanced Hydrogen Evolution in pH 0-14 Aqueous Solutions, ChemSusChem. 10 (2017) 4632–4641. https://doi.org/10.1002/cssc.201701196.

[48] J. Zemann, Crystal structures, 2 nd edition. Vol. 1 by R. W. G. Wyckoff, Acta Crystallogr. 18 (1965) 139–139. https://doi.org/10.1107/S0365110X65000361.

[49] F. Neese, Software update: the ORCA program system, version 4.0, Wiley Interdiscip. Rev. Comput. Mol. Sci. 8 (2018) 4–9. https://doi.org/10.1002/wcms.1327.

[50] A.D. Becke, Density-functional thermochemistry. III. The role of exact exchange, J. Chem. Phys. 98 (1993) 5648–5652. https://doi.org/10.1063/1.464913.

[51] C. Lee, W. Yang, R.G. Parr, Development of the Colle-Salvetti correlation-energy formula into a functional of the electron density, Phys. Rev. B. 37 (1988) 785–789. https://doi.org/10.1103/PhysRevB.37.785.

[52]   P.J. Hay, W.R. Wadt, Ab initio effective core potentials for molecular calculations. Potentials for K to Au including the outermost core orbitals, J. Chem. Phys. 82 (1985) 299–310. https://doi.org/10.1063/1.448975.

[53]   S. Grimme, J. Antony, S. Ehrlich, H. Krieg, A consistent and accurate ab initio parametrization of density functional dispersion correction (DFT-D) for the 94 elements H-Pu, J. Chem. Phys. 132 (2010) 154104. https://doi.org/10.1063/1.3382344.

[54]   S. Grimme, S. Ehrlich, L. Goerigk, Effect of the damping function in dispersion corrected density functional theory, J. Comput. Chem. 32 (2011) 1456–1465. https://doi.org/10.1002/jcc.21759.

[55]   P. Geerlings, F. De Proft, W. Langenaeker, Conceptual Density Functional Theory, Chem. Rev. 103 (2003) 1793–1874. https://doi.org/10.1021/cr990029p.

[56]   S.F. Boys, F. Bernardi, The calculation of small molecular interactions by the differences of separate total energies. Some procedures with reduced errors, Mol. Phys. 19 (1970) 553–566. https://doi.org/10.1080/00268977000101561.

[57]   C. Lefebvre, G. Rubez, H. Khartabil, J.-C. Boisson, J. Contreras-García, E. Hénon, Accurately extracting the signature of intermolecular interactions present in the NCI plot of the reduced density gradient versus electron density, Phys. Chem. Chem. Phys. 19 (2017) 17928–17936. https://doi.org/10.1039/C7CP02110K.

[58]   T. Lu, F. Chen, Multiwfn: A multifunctional wavefunction analyzer, J. Comput. Chem. 33 (2012) 580–592. https://doi.org/10.1002/jcc.22885.

[59]   L. Noodleman, E.R. Davidson, Ligand spin polarization and antiferromagnetic coupling in transition metal dimers, Chem. Phys. 109 (1986) 131–143. https://doi.org/10.1016/0301-0104(86)80192-6.

[60]   S.X. Cui, H.Y. Wang, J. Xu, J.P. Zhang, Theoretical studies on magnetic properties of a binuclear paddle wheel Cu(II) complex $\{Cu_2(\mu_2\text{-}O_2CCH_3)_4\}(OCNH_2CH_3)_2$, Russ. J. Phys. Chem. A. 91 (2017) 1070–1075. https://doi.org/10.1134/S0036024417060085.

[61]   J. Svorec, P. Polakovičová, J. Moncol, V. Kuchtanin, M. Breza, S. Šoralová, Z. Padělková, J. Mrozinski, T. Lis, P. Segľa, Structural, magnetic and quantum-chemical study of dinuclear copper(II) thiophenecarboxylate and furancarboxylate complexes, Polyhedron. 81 (2014) 216–226. https://doi.org/10.1016/j.poly.2014.05.071.

[62]   J.H. Van Vleck, Quantum mechanics-The key to understanding magnetism, Rev. Mod. Phys. 50 (1978) 181–189. https://doi.org/10.1103/RevModPhys.50.181.

[63]   C. Desplanches, E. Ruiz, S. Alvarez, Exchange coupling in metal complexes of the second transition series: A theoretical exploration, Eur. J. Inorg. Chem. (2003) 1756–1760. https://doi.org/10.1002/ejic.200200457.

[64]   E. Ruiz, J. Cirera, S. Alvarez, Spin density distribution in transition metal complexes, Coord. Chem. Rev. 249 (2005) 2649–2660. https://doi.org/10.1016/j.ccr.2005.04.010.

[65]   T. Cauchy, E. Ruiz, S. Alvarez, Magnetostructural correlations in polynuclear complexes: The Fe$_4$ butterflies, J. Am. Chem. Soc. 128 (2006) 15722–15727. https://doi.org/10.1021/ja0641498.

[66]   K. Muñoz-Becerra, D. Aravena, E. Ruiz, E. Spodine, N. Soto-Donoso, V. Paredes-García, D. Venegas-Yazigi, Models to predict the magnetic properties of single- and multiple-bridged phosphate Cu^{II} systems: A theoretical DFT insight, Inorg. Chem. Front. 4 (2017) 509–520. https://doi.org/10.1039/c6qi00394j.

[67]   A.K. Seguin, K. Wrighton-Araneda, D. Cortés-Arriagada, C. Cruz, D. Venegas-Yazigi, V. Paredes-García, A new Cu^{II}-dinuclear paddlewheel complex. Structural and

electronic properties, J. Mol. Struct. 1224 (2021) 129172. https://doi.org/10.1016/j.molstruc.2020.129172.

[68]   K. Yamaguchi, Y. Takahara, T. Fueno, Ab-Initio Molecular Orbital Studies of Structure and Reactivity of Transition Metal-OXO Compounds, in: Appl. Quantum Chem., Springer Netherlands, Dordrecht, 1986: pp. 155–184. https://doi.org/10.1007/978-94-009-4746-7_11.

[69]   T. Soda, Y. Kitagawa, T. Onishi, Y. Takano, Y. Shigeta, H. Nagao, Y. Yoshioka, K. Yamaguchi, Ab initio computations of effective exchange integrals for H–H, H–He–H and Mn_2O_2 complex: comparison of broken-symmetry approaches, Chem. Phys. Lett. 319 (2000) 223–230. https://doi.org/10.1016/S0009-2614(00)00166-4.

[70]   S. Alvarez, D. Avnir, M. Llunell, M. Pinsky, Continuous symmetry maps and shape classification. The case of six-coordinated metal compoundsElectronic supplementary information (ESI) available: tables of CSD refcodes, structural parameters and symmetry measures for the studied compounds. See http://w, New J. Chem. 26 (2002) 996–1009. https://doi.org/10.1039/b200641n.

[71]   S. Alvarez, M. Llunell, Continuous symmetry measures of penta-coordinate molecules: Berry and non-Berry distortions of the trigonal bipyramid †, J. Chem. Soc. Dalt. Trans. (2000) 3288–3303. https://doi.org/10.1039/b004878j.

[72]   G. Pomarico, S. Nardis, R. Paolesse, O.C. Ongayi, B.H. Courtney, F.R. Fronczek, M.G.H. Vicente, Synthetic Routes to 5,10,15-Triaryl-tetrabenzocorroles, J. Org. Chem. 76 (2011) 3765–3773. https://doi.org/10.1021/jo200026u.

[73]   M. Hoffmann, B. Cordes, C. Kleeberg, P. Schweyen, B. Wolfram, M. Bröring, Template Synthesis of Alkyl-Substituted Metal Isocorroles, Eur. J. Inorg. Chem. 2016 (2016) 3076–3085. https://doi.org/10.1002/ejic.201600419.

[74]   S. Will, J. Lex, E. Vogel, H. Schmickler, J.-P. Gisselbrecht, C. Haubtmann, M. Bernard, M. Gorss, Nickel and Copper Corroles: Well-Known Complexes in a New Light, Angew. Chemie Int. Ed. English. 36 (1997) 357–361. https://doi.org/10.1002/anie.199703571.

[75]   C. Brückner, R.P. Briñas, J.A. Krause Bauer, X-ray Structure and Variable Temperature NMR Spectra of [m eso -Triarylcorrolato]copper(III), Inorg. Chem. 42 (2003) 4495–4497. https://doi.org/10.1021/ic034080u.

[76]   F. Wu, J. Liu, P. Mishra, T. Komeda, J. Mack, Y. Chang, N. Kobayashi, Z. Shen, Modulation of the molecular spintronic properties of adsorbed copper corroles, Nat. Commun. 6 (2015) 7547. https://doi.org/10.1038/ncomms8547.

[77]   K.E. Thomas, H. Vazquez-Lima, Y. Fang, Y. Song, K.J. Gagnon, C.M. Beavers, K.M. Kadish, A. Ghosh, Ligand Noninnocence in Coinage Metal Corroles: A Silver Knife-Edge, Chem. - A Eur. J. 21 (2015) 16839–16847. https://doi.org/10.1002/chem.201502150.

[78]   K. Sudhakar, A. Mahammed, N. Fridman, Z. Gross, Trifluoromethylation for affecting the structural, electronic and redox properties of cobalt corroles, Dalt. Trans. 48 (2019) 4798–4810. https://doi.org/10.1039/C9DT00675C.

[79]   H. Lei, H. Fang, Y. Han, W. Lai, X. Fu, R. Cao, Reactivity and Mechanism Studies of Hydrogen Evolution Catalyzed by Copper Corroles, ACS Catal. 5 (2015) 5145–5153. https://doi.org/10.1021/acscatal.5b00666.

[80]   M. Soll, K. Sudhakar, N. Fridman, A. Müller, B. Röder, Z. Gross, One-Pot Conversion of Fluorophores to Phosphorophores, Org. Lett. 18 (2016) 5840–5843. https://doi.org/10.1021/acs.orglett.6b02877.

[81]   E. Ruiz, A. Rodríguez-Fortea, J. Tercero, T. Cauchy, C. Massobrio, Exchange coupling in transition-metal complexes via density-functional theory: Comparison and reliability of different basis set approaches, J. Chem. Phys. 123 (2005). https://doi.org/10.1063/1.1999631.

[82]   S. Jana, P. Aich, P.A. Kumar, O.K. Forslund, E. Nocerino, V. Pomjakushin, M. Månsson, Y. Sassa, P. Svedlindh, O. Karis, V. Siruguri, S. Ray, Revisiting Goodenough-Kanamori rules in a new series of double perovskites $LaSr_{1-x}Ca_xNiReO_6$, Sci. Rep. 9 (2019) 1–10. https://doi.org/10.1038/s41598-019-54427-0.

[83]   Y. Naruse, A. Takamori, Orbital Phase Perspective of Goodenough-Kanamori-Anderson Rules (GKA Rules) in Superexchange Interaction, ChemRxiv. (2021).

[84]   S. Ooi, T. Tanaka, T. Ikeue, K. Yamasumi, K. Ueta, D. Shimizu, M. Ishida, H. Furuta, A. Osuka, Bis-copper(II) Complex of Triply-linked Corrole Dimer and Its Dication, Chem. – An Asian J. 14 (2019) 1771–1776. https://doi.org/10.1002/asia.201801467.

[85]   S. Ganguly, A. Ghosh, Seven Clues to Ligand Noninnocence: The Metallocorrole Paradigm, Acc. Chem. Res. 52 (2019) 2003–2014. https://doi.org/10.1021/acs.accounts.9b00115.

[86]   C.I.M. Santos, L. Rodríguez-Pérez, G. Gonçalves, S.N. Pinto, M. Melle-Franco, P.A.A.P. Marques, M.A.F. Faustino, M.Á. Herranz, N. Martin, M.G.P.M.S. Neves, J.M.G. Martinho, E.M.S. Maçôas, Novel hybrids based on graphene quantum dots covalently linked to glycol corroles for multiphoton bioimaging, Carbon N. Y. 166 (2020) 164–174. https://doi.org/10.1016/j.carbon.2020.04.012.

[87]   M. Paszkiewicz, T. Biktagirov, H. Aldahhak, F. Allegretti, E. Rauls, W. Schöfberger, W.G. Schmidt, J. V. Barth, U. Gerstmann, F. Klappenberger, Unraveling the Oxidation and Spin State of Mn–Corrole through X-ray Spectroscopy and Quantum Chemical Analysis, J. Phys. Chem. Lett. 9 (2018) 6412–6420. https://doi.org/10.1021/acs.jpclett.8b02525.

[88]   M. Zugermeier, J. Herritsch, J.-N. Luy, M. Chen, B.P. Klein, F. Niefind, P. Schweyen, M. Bröring, M. Schmid, R. Tonner, J.M. Gottfried, On-Surface Formation of a Transient Corrole Radical and Aromaticity-Driven Interfacial Electron Transfer, J. Phys. Chem. C. 124 (2020) 13825–13836. https://doi.org/10.1021/acs.jpcc.0c04451.

[89]   J. Xu, L. Zhu, H. Gao, C. Li, M. Zhu, Z. Jia, X. Zhu, Y. Zhao, S. Li, F. Wu, Z. Shen, Ligand Non-innocence and Single Molecular Spintronic Properties of Ag II Dibenzocorrole Radical on Ag(111), Angew. Chemie Int. Ed. 60 (2021) 11702–11706. https://doi.org/10.1002/anie.202016674.

[90]   D.P. Miller, J. Hooper, S. Simpson, P.S. Costa, N. Tymińska, S.M. McDonnell, J.A. Bennett, A. Enders, E. Zurek, Electronic Structure of Iron Porphyrin Adsorbed to the Pt(111) Surface, J. Phys. Chem. C. 120 (2016) 29173–29181. https://doi.org/10.1021/acs.jpcc.6b09408.

[91]   N. Saikia, M. Seel, R. Pandey, Stability and Electronic Properties of 2D Nanomaterials Conjugated with Pyrazinamide Chemotherapeutic: A First-Principles Cluster Study, J. Phys. Chem. C. 120 (2016) 20323–20332. https://doi.org/10.1021/acs.jpcc.6b06000.

[92]   J. Tang, B. Chen, Y. Zhang, J. Lu, T. Zhang, Q. Guo, J. Zhang, Synthesis and gas sensitivity properties of novel metallocorroles and functionalized graphene oxide, Funct. Mater. Lett. 12 (2019) 1940001. https://doi.org/10.1142/S1793604719400010.

[93]   S. Tebi, M. Paszkiewicz, H. Aldahhak, F. Allegretti, S. Gonglach, M. Haas, M. Waser, P.S. Deimel, P.C. Aguilar, Y.-Q. Zhang, A.C. Papageorgiou, D.A. Duncan, J. V.

Barth, W.G. Schmidt, R. Koch, U. Gerstmann, E. Rauls, F. Klappenberger, W. Schöfberger, S. Müllegger, On-Surface Site-Selective Cyclization of Corrole Radicals, ACS Nano. 11 (2017) 3383–3391. https://doi.org/10.1021/acsnano.7b00766.

[94]   Y.-W. Son, M.L. Cohen, S.G. Louie, Half-metallic graphene nanoribbons, Nature. 444 (2006) 347–349. https://doi.org/10.1038/nature05180.

[95]   Z.F. Wang, S. Jin, F. Liu, Spatially separated spin carriers in spin-semiconducting graphene nanoribbons, Phys. Rev. Lett. 111 (2013) 1–5. https://doi.org/10.1103/PhysRevLett.111.096803.

[96]   A. Mugarza, C. Krull, R. Robles, S. Stepanow, G. Ceballos, P. Gambardella, Spin coupling and relaxation inside molecule–metal contacts, Nat. Commun. 2 (2011) 490. https://doi.org/10.1038/ncomms1497.

[97]   T.Y. Yang, J. Balakrishnan, F. Volmer, A. Avsar, M. Jaiswal, J. Samm, S.R. Ali, A. Pachoud, M. Zeng, M. Popinciuc, G. Güntherodt, B. Beschoten, B. Özyilmaz, Observation of Long Spin-Relaxation Times in Bilayer Graphene at Room Temperature, Phys. Rev. Lett. 107 (2011) 047206. https://doi.org/10.1103/PhysRevLett.107.047206.

[98]   W. Han, R.K. Kawakami, Spin Relaxation in Single-Layer and Bilayer Graphene, Phys. Rev. Lett. 107 (2011) 047207. https://doi.org/10.1103/PhysRevLett.107.047207.

[99]   B. Dlubak, M.-B. Martin, C. Deranlot, B. Servet, S. Xavier, R. Mattana, M. Sprinkle, C. Berger, W.A. De Heer, F. Petroff, A. Anane, P. Seneor, A. Fert, Highly efficient spin transport in epitaxial graphene on SiC, Nat. Phys. 8 (2012) 557–561. https://doi.org/10.1038/nphys2331.

[100]   F.J. Jedema, A.T. Filip, B.J. van Wees, Electrical spin injection and accumulation at room temperature in an all-metal mesoscopic spin valve, Nature. 410 (2001) 345–348. https://doi.org/10.1038/35066533.

[101]   T. Yang, T. Kimura, Y. Otani, Giant spin-accumulation signal and pure spin-current-induced reversible magnetization switching, Nat. Phys. 4 (2008) 851–854. https://doi.org/10.1038/nphys1095.

[102]   F.J. Jedema, H.B. Heersche, A.T. Filip, J.J.A. Baselmans, B.J. van Wees, Electrical detection of spin precession in a metallic mesoscopic spin valve, Nature. 416 (2002) 713–716. https://doi.org/10.1038/416713a.

[103]   H. Idzuchi, Y. Fukuma, L. Wang, Y. Otani, Spin relaxation mechanism in silver nanowires covered with MgO protection layer, Appl. Phys. Lett. 101 (2012) 022415. https://doi.org/10.1063/1.4737001.

[104]   T. Suzuki, T. Sasaki, T. Oikawa, M. Shiraishi, Y. Suzuki, K. Noguchi, Room-Temperature Electron Spin Transport in a Highly Doped Si Channel, Appl. Phys. Express. 4 (2011) 023003. https://doi.org/10.1143/APEX.4.023003.

[105]   I. Appelbaum, B. Huang, D.J. Monsma, Electronic measurement and control of spin transport in silicon, Nature. 447 (2007) 295–298. https://doi.org/10.1038/nature05803.

[106]   W. Han, R.K. Kawakami, M. Gmitra, J. Fabian, Graphene spintronics, Nat. Nanotechnol. 9 (2014) 794–807. https://doi.org/10.1038/nnano.2014.214.

[107]   E.C. Ahn, 2D materials for spintronic devices, Npj 2D Mater. Appl. 4 (2020). https://doi.org/10.1038/s41699-020-0152-0.

[108]   Y. Liu, C. Zeng, J. Zhong, J. Ding, Z.M. Wang, Z. Liu, Spintronics in Two-Dimensional Materials, Nano-Micro Lett. 12 (2020) 1–26. https://doi.org/10.1007/s40820-020-00424-2.

[109]   W. Liu, Y. Xu, Spintronic 2D Materials, Elsevier, 2020. https://doi.org/10.1016/C2016-0-03709-9.

[110] B. Yan, X. Li, J. Zhao, Z. Jia, F. Tang, Z. Zhang, D. Yu, K. Liu, L. Zhang, X. Wu, Gate tunable Kondo effect in magnetic molecule decorated graphene, Solid State Commun. 278 (2018) 24–30. https://doi.org/10.1016/j.ssc.2018.05.001.

[111] A. Kurzmann, Y. Kleeorin, C. Tong, R. Garreis, A. Knothe, M. Eich, C. Mittag, C. Gold, F.K. de Vries, K. Watanabe, T. Taniguchi, V. Fal'ko, Y. Meir, T. Ihn, K. Ensslin, Kondo effect and spin–orbit coupling in graphene quantum dots, Nat. Commun. 12 (2021) 6004. https://doi.org/10.1038/s41467-021-26149-3.

[112] J. Puebla, J. Kim, K. Kondou, Y. Otani, Spintronic devices for energy-efficient data storage and energy harvesting, Commun. Mater. 1 (2020) 24. https://doi.org/10.1038/s43246-020-0022-5.

[113] A. Kaidatzis, S. Sidorenko, I. Vladymyrskyi, D. Niarchos, Modern Magnetic and Spintronic Materials, Springer Netherlands, Dordrecht, 2020. https://doi.org/10.1007/978-94-024-2034-0.

[114] B. Wang, X. Zuo, Y. Wu, Z. Chen, C. He, W. Duan, Comparative gas sensing in copper porphyrin and copper phthalocyanine spin-coating films, Sensors Actuators B Chem. 152 (2011) 191–195. https://doi.org/10.1016/j.snb.2010.12.006.